ORIGINAL PAPER

Preparation and compression behavior of Fe–Ni–P/porous-Fe/Fe–Ni–P composites

Yu-xuan Liu[1] · Shuai-jiang Yan[1] · Cheng-song Zhang[1,2] · Da-zhi Chen[1,2] · Qin Xu[1] · Guo-dong Cui[1,2]

Abstract

Porous-Fe–N alloys designed for light weight or energy absorption are inevitably facing the compromise of deteriorated mechanical properties. To optimize their mechanical properties, here a novel Fe–Ni–P/porous-Fe/Fe–Ni–P composite with sandwich structure was fabricated by spark plasma sintering and further strengthened via cryogenic treatment. Based on the principle of solid phase sintering and transient liquid phase sintering, porous core and dense outer layers formed simultaneously after co-sintering. The as-fabricated samples show excellent compressive strength of 1708 MPa, and after cryogenic treatment, due to the sufficient martensitic transformation, Fe–Ni–P outer layers show substantially increased hardness from 246.7 to 386.6 $HV_{0.1}$ while the porous-Fe core remains unchanged. And the compressive strength maintains 1424 MPa despise the aggravated incongruity of deformation. The ratio of constituent microhardness R has been proposed to represent the hardness matching, and with decreasing R, the incongruity of deformation is intensified, and the nominal compressive strength is reduced.

Keywords Metallic composite · Sandwich structure · Spark plasma sintering · Mechanical property

1 Introduction

Porous metals got widely concerned due to their unique performance such as energy absorption and low density [1]. In the past decades, various porous materials, such as porous aluminum alloy, porous nickel alloy, porous titanium alloy and porous iron alloy, have been widely used in vehicle, aerospace, biomedical and other fields [1–4]. Recent years, using Fe–N powder as raw material, porous ferroalloy with micro-nano porous structure and excellent mechanical properties was prepared by spark plasma sintering (SPS) [5]. However, the main phase of the sintered samples changed from iron nitrogen compounds to α-Fe during sintering, the phase transition and porosity lead to

the degradation of surface hardness and corrosion resistance, consequently restricting their applications as precision powder metallurgy parts. Previous research has proposed carburizing surface treatment, and consequently, the mechanical properties have been significantly improved, but the corrosion resistance still needs to be further improved [6].

To modify the performance of such materials, sandwich structures with a porous metal core and a variety of dense surface are widely considered [1, 7–9]. Based on this concept, aluminum foam sandwich panels have got mature development and application, but there are limited studies on iron-based materials.

On the other hand, a kind of Fe–Ni–P composite powder has been developed for transient liquid phase sintering to prepare iron-based alloy with relatively low sintering temperature [10]. By strictly controlling the content of Ni in the preparation process, an Fe–Ni–P alloy with metastable γ phase matrix can be obtained, which can improve the plasticity of the alloy without degrading the higher hardness and strength [11]. Moreover, transformation from metastable γ phase into α phase via cryogenic treatment could significantly improve the comprehensive

✉ Guo-dong Cui
  gdcui@swjtu.edu.cn

[1] Key Lab of Advanced Technology of Materials of Education Ministry, School of Materials Science and Engineering, Southwest Jiaotong University, Chengdu 610031, Sichuan, China

[2] Yibin Institute of Southwest Jiaotong University, Yibin 644000, Sichuan, China

mechanical properties [12]. Such sintered alloy could get sufficient densification with low temperature that will not eliminate the pores of sintered Fe–N alloy. Thus in this study, the co-sintering of layered-filled Fe–N powder and Fe–Ni–P composite powder has been proposed to prepare Fe–Ni–P/porous-Fe/Fe–Ni–P composite with sandwich structures. And cryogenic treatment has been carried out for further strengthen. This study will provide an important reference for the further development and application of the composites in precision parts (gears and bearings) of powder metallurgy.

2 Experimental

2.1 Preparation of Fe–Ni–P/porous-Fe/Fe–Ni–P composites

Figure 1 illustrates the main preparation processes of Fe–Ni–P/porous-Fe/Fe–Ni–P composites. As reported in previous works, Fe–N powder was synthesized by ammonia reduction and nitriding at 650 °C for 4 h using the iron oxide powder (99.5% purity, 200 nm in average size,

Chengdu Jing Ke Materials Co., Ltd., China) as the raw material, and the as-prepared Fe–N powder has a hollow structure with the main composition of $Fe_{2-3}N$ [5], while Fe–Ni–P composite powder was prepared by electroless plating to achieve Ni–P coating on the surface of carbonyl iron powder (99.7% purity, 8 μm in average size, Beijing Xing Rong Yuan Technology Co., Ltd., China). For the preparation of the bath solution, 30 g nickel sulfate ($NiSO_4 \cdot 6H_2O$), 25 g sodium hypophosphite ($NaH_2PO_2 \cdot H_2O$), 15 g sodium acetate ($CH_3COONa \cdot 3H_2O$), 10 g sodium citrate ($Na_3C_6H_5O_7 \cdot 2H_2O$) and 10 mL lactic acid ($C_3H_6O_3$) were dissolved in 1000 mL distilled water, and pH value had been regulated to 6 by adding ammonia water before plating. The raw powder was immersed into the bath solution and plated at 75 °C for 1 h followed by cleaning and drying procedures. Fe–Ni–P composite powder shows a spherical morphology covered with Ni–P coating [11], and the chemical composition was measured to be Fe 65.67, Ni 29.68 and P 4.51 (in wt.%) by means of X-ray fluorescence spectrometry (XRF-1800).

Then, the as-prepared Fe–N powder and Fe–Ni–P composite powder were poured into a graphite die with an inner diameter of 20 mm and a height of 60 mm by
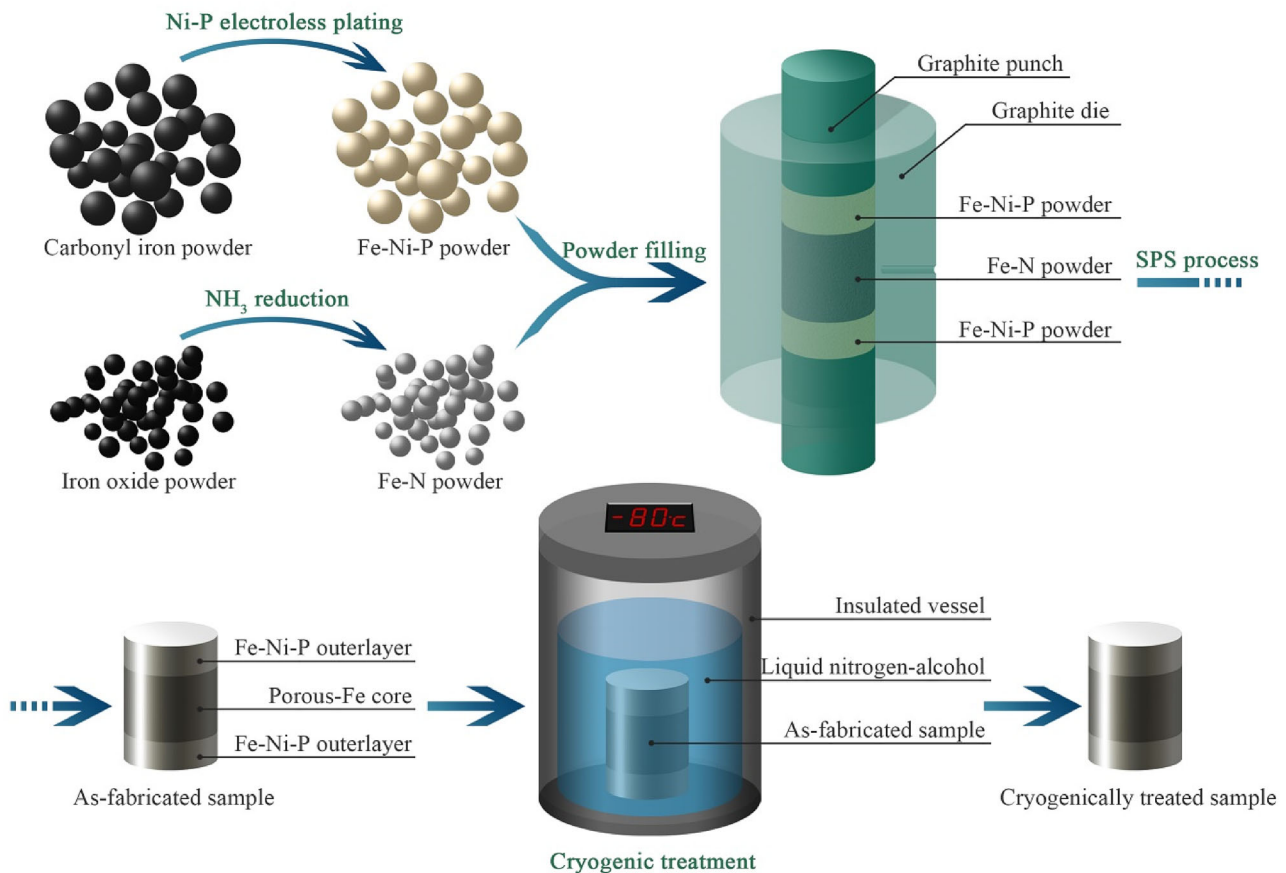

Fig. 1 Schematic illustration of preparation processes of Fe–Ni–P/porous-Fe/Fe–Ni–P composites

sequence as shown in Fig. 1. The graphite die was pre-lined with 0.15-mm-thick graphite paper to separate the mold from the powder, to avoid mold damage due to the direct contact between powder and mold during sintering. Each side of the powder compact contains 10 g Fe–Ni–P composite powder while 20 g Fe–N powder was loaded in the inner part of the die. After that, the powder compact was pre-pressed with the load of 10 MPa at room temperature, and then sintered using an SPS system (model HD-10 from FCT Germany) at the temperature of 875 °C soaking for 5 min under pressure of 20 MPa. Finally, for the cryogenic treatment, the as-fabricated samples were placed in liquid nitrogen that had been previously adjusted to − 80 °C by adding alcohol and treated for 15 min to achieve the martensite transformation.

2.2 Characterization

Before the microstructure characterization, all samples were ground with SiC paper to remove residual graphite paper. And the samples were polished and etched by using the Kalling reagent (100 mL ethanol, 100 mL hydrochloric acid and 5 g copper chloride) for 20 s to prepare metallographic samples. A field emission scanning electron microscopy (FE-SEM, JSM-7001F, JEOL, Japan) equipped with energy dispersive X-ray spectroscopy (EDS) was used to complete the metallography and composition characterization. The phases of the sintered samples were characterized by X-ray diffraction (X′ pert pro XRD, PANalytical Co., Netherlands) with Cu Kα radiation, while the scanning range was adjusted in the range of 20°–90°.

The Vickers hardness was measured using a digital microhardness tester (HV, Laizhou Huayin Testing Instrument Co., Ltd., China) under a load of 0.98 N for 15 s. Compressive properties of the samples were tested on the electronic universal materials testing machine (WDW-200, Changchun Kexin Test Instrument Co., Ltd., China) with a strain rate of 1 mm min^{-1}. In the compressive tests, cylinders were cut from the samples using the EDM machine with a diameter of 8 mm and a height of 12 mm as suggested in ASTM E9-98a(2000) standard.

3 Results and discussion

3.1 Microstructure of Fe–Ni–P/porous-Fe/Fe–Ni–P composites

Figure 2 shows the cross-sectional microstructure of the as-fabricated samples. In the porous-Fe part (see Fig. 2a), round-shaped micro pores are uniformly distributed as a result of the emission of nitrogen gas, and with the help of X-ray diffraction (XRD) analysis, the main composition is

determined to be α-Fe for the complete decomposition of iron nitride [5]. With the supplementary of height maps (see Fig. 2g), the porous-Fe part shows rough plane, which further reveals a porous structure. As for Fe–Ni–P part (see Fig. 2c), according to Fe–Ni binary phase diagram, the major composition of this part under current chemical composition should be α and γ phase. In fact, during the cooling stage of SPS process, γ → α + γ equilibrium transformation was substantially inadequate because the equilibrium microstructure only can be formed under extremely slow cooling rate [13]. Thus, XRD results shows dominant γ phase, while the content of α phase is too negligible to be detected in the metallographic analysis. And it is certain that most of γ phases formed during soaking stage are retained after cooling and in metastable state under ambient temperature. On the other hand, the scatter marked by the arrow is determined to be phosphide in form of (Fe, Ni)$_3$P, which has been reported in many relevant studies [10, 11, 14]. Although XRD pattern shows no corresponding characteristic signal due to the low content and dispersive distribution, the height map of Fe–Ni–P part (see Fig. 2g) shows a smooth surface, indicating a dense microstructure.

As can be observed from Fig. 2b, complete combination has been achieved by SPS at the interface between layers. EDS maps (see Fig. 2d–f) show that Ni is in gradient distribution along the direction vertical to the interface, while P concentration is comparatively uniform in this scale, which indicates that the diffusion of P is more adequate. Meanwhile, as marked by arrow, there are P-concentrated areas detected, which indicates the formation of phosphates precipitation.

Figure 3 shows the micromorphology of the cryogenically treated samples. Fe–Ni–P outer layers have undergone obvious martensitic transformation from face centered cubic-γ-Fe–Ni–P to body centered cubic (BCC)-α-Fe–Ni–P phase (see Fig. 3c). As marked by the arrows in Fig. 3c, the martensitic appears in acicular shape and zig-zag distribution. XRD result shown in Fig. 3e also indicates that most of the metastable γ phases have been transformed into α phase. Related research shows that the martensitic transformation of metastable γ phase in Fe–Ni system belongs to diffusionless type, and compared with binary Fe–Ni alloy, the martensitic transformation of the current Fe–Ni–P alloy with similar Ni content is more adequate [15], which indicates that the doping of P can further improve the instability of γ phase and make the cryogenic strengthening easier to achieve. However, as can be observed from Fig. 3b, near the interface, Fe–Ni–P side shows no obvious change. It is because this region contains less Ni due to the element diffusion across the interface. According to Fe–Ni–P phase diagram [13], there could be more α phase formed with low Ni concentration. Thus, in
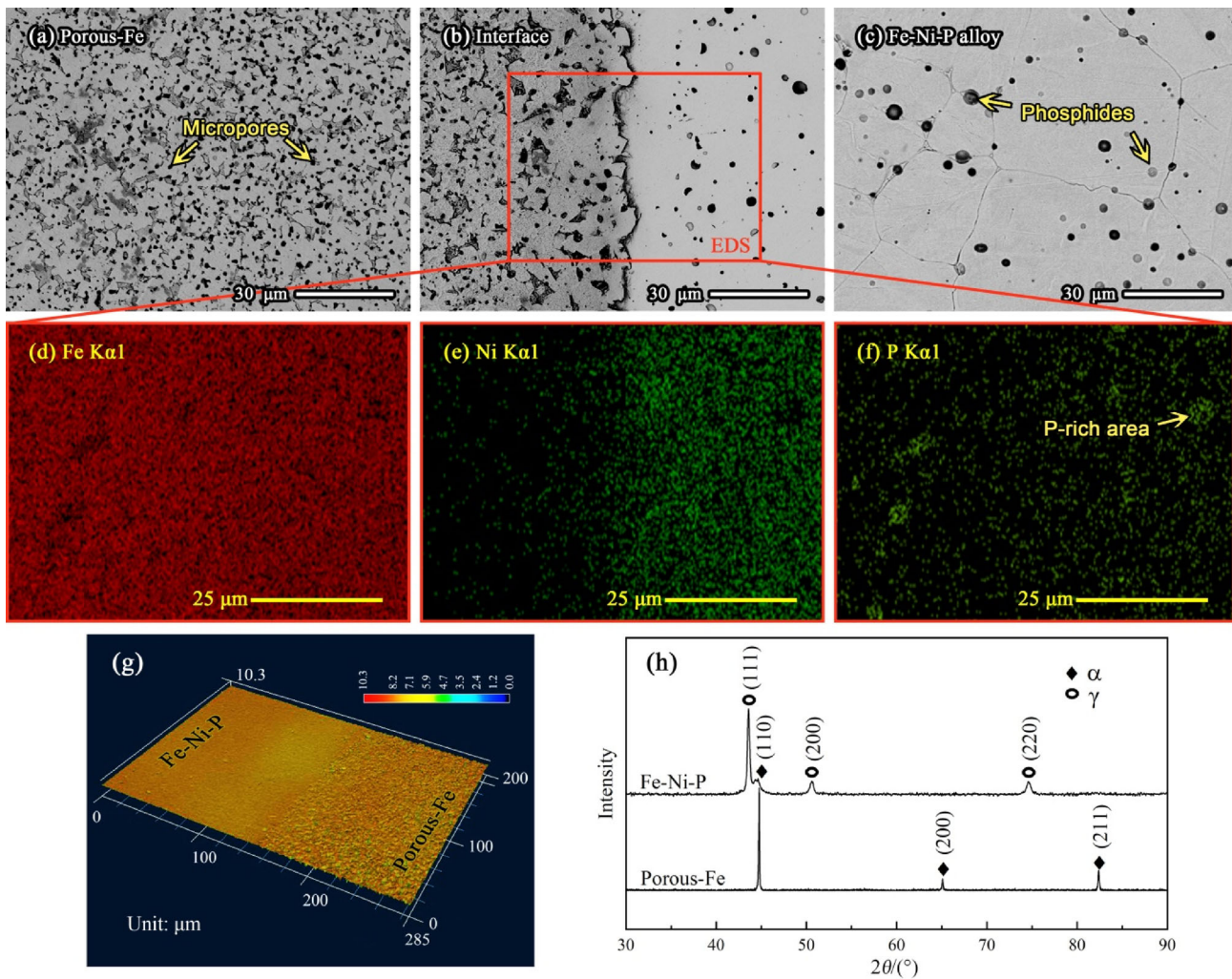
Fig. 2 SEM micrographs of as-fabricated samples (**a–c**), EDS maps (**d–f**) and height map of interface in **b** (**g**), and XRD patterns of constituents (**h**). **a** Porous-Fe part; **b** interface; **c** Fe–Ni–P part; **d** Fe; **e** Ni; **f** P. θ Bragg angle

this area, α phase pre-existed and did not transform during cryogenic treatment. While as reported, the elements distribution and precipitates arrangement did not change significantly during the martensitic transformation due to the non-diffusion phase transition in which the atoms in Fe–Ni–P alloys are displaced through shearing rather than migration [12]. Meanwhile, the porous-Fe matrix shows no obvious change, and XRD result shows that BCC structure remains unchanged after cryogenic treatment. The height maps indicate that the porous structure retained and no cracks generated along the interface or in the matrix after cryogenic treatment. Since the phase cross the interface arranges in gradient, martensitic transformation did not occur in the pre-existed α phase region adjacent to the interface, which is of significance to the avoidance of cracks along the interface.

3.2 Sintering behavior of Fe–Ni–P/porous-Fe/Fe–Ni–P composites

During the sintering process, Fe–N powder follows solid phase sintering while Fe–Ni–P powder is subjected to transient liquid phase sintering. As reported in Ref. [5], Fe–N powder decomposed during sintering with the release of nitrogen. And with the formation and growth of sintering neck, part of the nitrogen was trapped in these formed closed pores, which is an inhibiting factor of densification [16, 17]. And the elimination of pores and densification at final sintering stage could be described by the model of Markworth [18]:

$$\frac{\mathrm{d}\rho}{\mathrm{d}t} = \frac{12\Omega D}{kTG^2}\left[P_{\mathrm{eff}} + \frac{2\gamma}{r} - P_{\mathrm{G}}\right] \tag{1}$$

where $\mathrm{d}\rho/\mathrm{d}t$ represents the densification rate; Ω is the atomic volume; D is the diffusivity; k is the Boltzmann
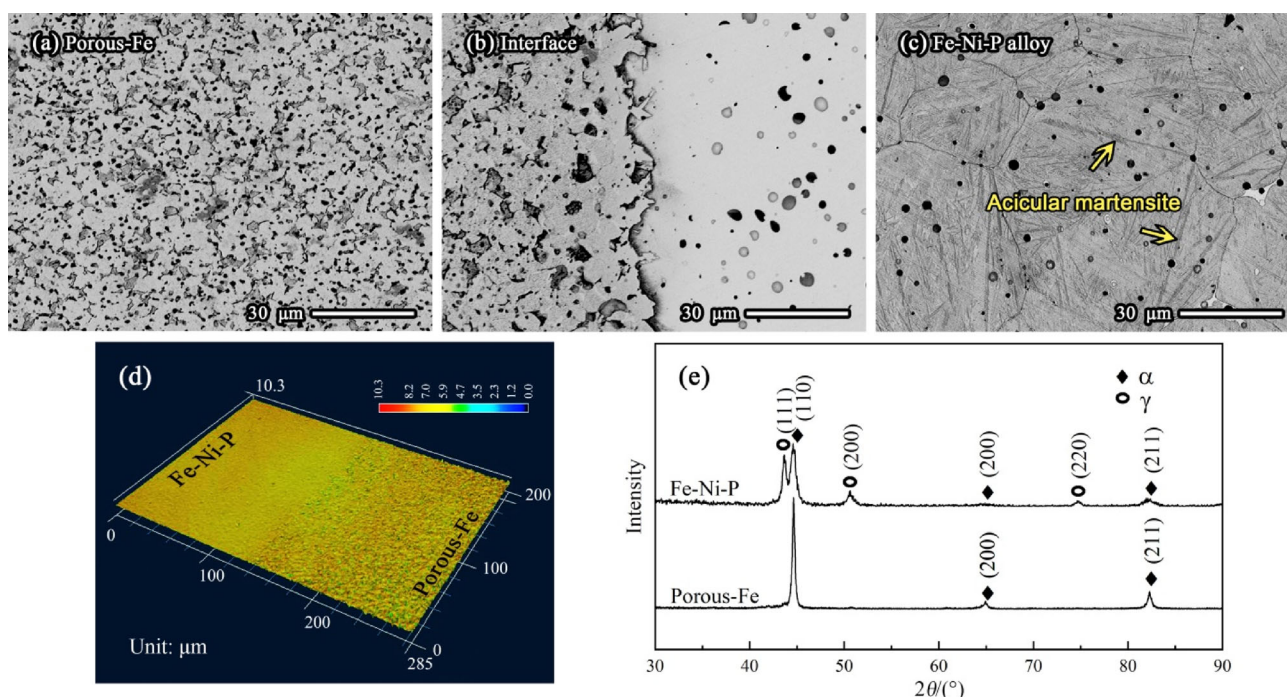
Fig. 3 SEM micrographs of cryogenically treated samples (**a–c**), height map of interface (**d**) and XRD patterns of constituents (**e**). **a** Porous-Fe part; **b** interface; **c** Fe–Ni–P part

constant; T is the absolute temperature; G is the grain size; P_{eff} is the effective applied pressure within the solid; γ is the mean surface energy; r is the radius of the pores; and P_G is the gas pressure in the pores. Obviously, the densification will end when the gas pressure in pores is increased enough to counterbalance the driving force. Thus, pores are difficult to be eliminated by effective pressure, and porous structure could be formed.

As for the sintered Fe–Ni–P composite powder, a dense structure tends to form as a result of transient liquid phase sintering process which could be typically divided into several stages: preliquid stage, incipient liquid formation stage, solution–reprecipitation stage and solid phase sintering stage [19]. In this study, abundant additive in carbonyl iron powder appears in the form of coating, which promotes the elimination of pores and densification by introducing sufficient liquid phase uniformly distributed between contact surfaces of particles [20].
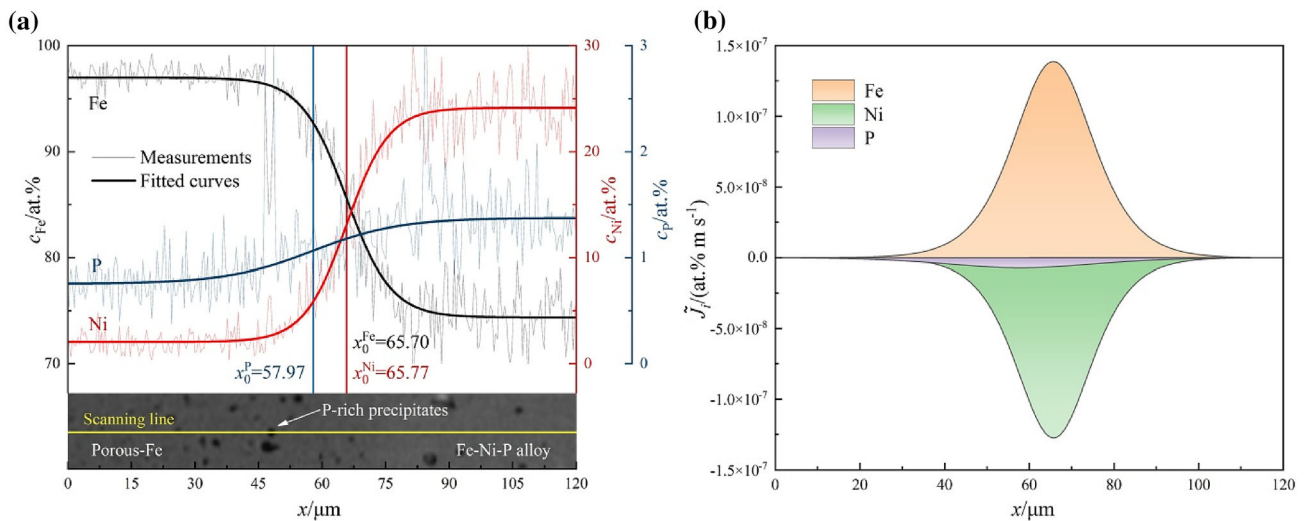
Concentration profile of components cross the interface was calculated by EDS and is plotted in Fig. 4a. To make the concentration profile smooth enough for further calculations, Boltzmann fitting was applied, and well-fitted curves were obtained and are depicted by the thick lines. And the Matano planes of constituents are determined by Ref. [21]:

$$\int_{c_i^-}^{c_i^+} (x - x_0)\mathrm{d}c_i = 0 \; (i = 1, 2) \tag{2}$$

where c_i denotes the concentration of component i; c_i^- and c_i^+ are the terminal concentrations; and x and x_0 denote the distance and the position of the Matano plane, respectively. As the result shows, the Matano planes of Fe and Ni almost coincide with each other while those of P get significant left deviation, which could be explained by the transitional liquid phase sintering behavior. With the solution-reprecipitation process continuing, the content of phosphorus in the liquid phase increases gradually, and then the liquid phase with higher phosphorus flows through the boundary into Fe–N powder side, causing the left offset of the Matano plane of P. As arrowed in Fig. 4a, P-rich precipitates detected in the porous-Fe side also confirm such rearrangement of the liquid phase. Moreover, the interdiffusion flux $\tilde{J}_i$ at any given position x^* could be calculated by [21]:

$$\tilde{J}_i(x^*) = \frac{1}{2t} \int_{c_i^+ \; or \; c_i^-}^{c_i(x^*)} (x - x_0)\mathrm{d}c_i \; (i = 1, 2) \tag{3}$$

where t is the diffusion time; and $c_i(x^*)$ denotes the concentration at position x^*. Thus, the results of calculation were plotted in Fig. 4b. It can be seen that the interdiffusion flux of Fe is positive while that of Ni and P is negative,

Fig. 4 Concentration profile of interface components measured by EDS (denoted by light line) and Boltzmann fitted curves (denoted by dark line) (**a**) and interdiffusion flux profile of components at interface (**b**)

indicating opposite diffusion direction of Fe with Ni and P. $\tilde{J}_{Fe}$ approximately equals to sum of $\tilde{J}_{Ni}$ and $\tilde{J}_{P}$, which means that the total flux of atoms in the diffusion system is in equilibrium during the diffusion process. Also it can be inferred that there was no Kirkendall hole formed during interface diffusion, which is of great significance for good interface combination.

3.3 Mechanical properties of Fe–Ni–P/porous-Fe/Fe–Ni–P composites

Figure 5a shows the microhardness profiles of the as-fabricated and the cryogenically treated samples. For the as-fabricated samples, the average hardness of Fe–Ni–P and porous-Fe matrix was measured to be 246.7 and 179.9

$HV_{0.1}$, respectively. The relatively higher hardness of outer layers can effectively improve the surface mechanical properties of the composite material. The maximum hardness (353.6 $HV_{0.1}$) is obtained in area I, which is in accordance with Ni-poor area. It is further proved that more α phase forms in this area and results in the improvement of hardness. The microhardness of the porous-Fe side in the area II is higher than that of the porous-Fe matrix. As described previously, the infiltration of P-rich liquid phase into porous-Fe layer during sintering could also leads to the densification of these infiltrated areas, which contributes to the increase in hardness. While combining the micrographs shown in Fig. 2b or Fig. 3b, the depth has been estimated to be within 20 μm, which is smaller than the range of total region II. The hardening of
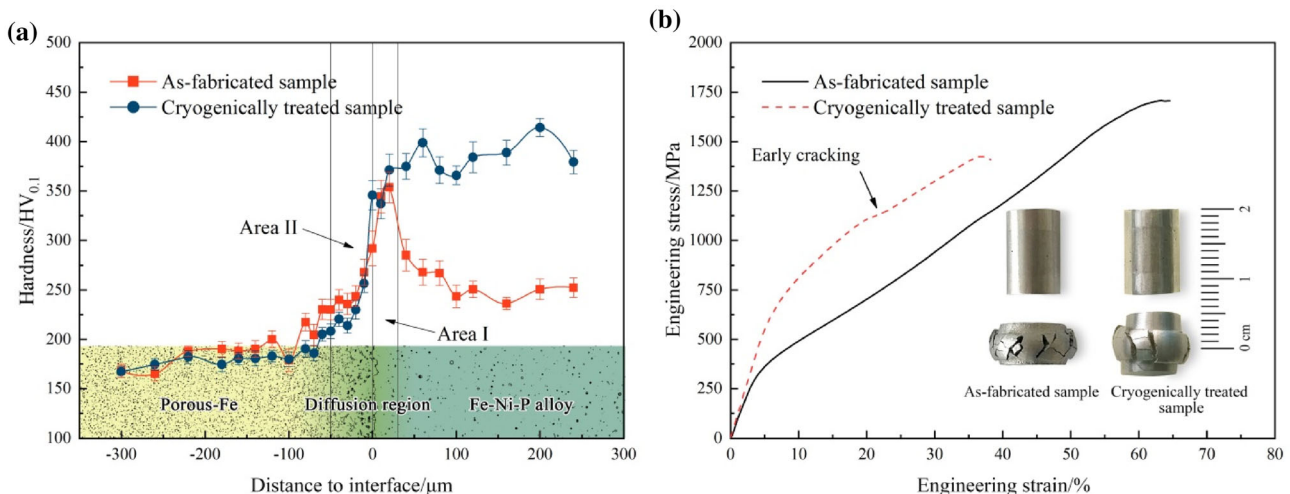
Fig. 5 Microhardness profiles (**a**) and compressive stress–strain curves (**b**) of as-fabricated samples and cryogenically treated samples

the rest of region II mainly comes from the solution strengthening effect of P diffused into the porous-Fe part. As reported, with increasing P content in a range, the hardness of Fe-P ferroalloys could be improved [22], and thus, there appears hardness gradient along with P concentration gradient.

After cryogenic treatment, the hardness of Fe–Ni–P matrix was improved from 246.7 to 386.6 $HV_{0.1}$ due to the martensite phase transformation. However, in area I, hardness has not changed significantly, which indicates that α phase pre-exists and remains unchanged after cryogenic treatment. And the average hardness of the porous-Fe matrix was measured to be 175.8 $HV_{0.1}$ which is essentially the same as that of the as-fabricated samples. Thus, the cryogenic treatment could significantly improve the mechanical properties of Fe–Ni–P outer layers, but has no obvious effect on the porous-Fe core.

As shown in Fig. 5b, in the compression test, final fracture occurred in the porous-Fe core for both of the samples due to the relatively poor mechanical properties, and multi-cracks without obvious orientation reveals plastic fracture. After cryogenic treatment, 0.2% offset yield strength is improved significantly by the cryogenic treatment, which might be explained as: Fe–Ni–P outer layers become much more rigid and difficult to deform, so that the porous-Fe core gets larger training rate compared with that of the as-fabricated samples, and under higher strain rate, the ferroalloys tend to be harder [23]. However, the compressive strength of the composite dropped from 1708 to 1424 MPa after cryogenic treatment, which could be attributed to the aggravated discrepancy of mechanical properties between layers. In this study, the ratio of components hardness (R) has been proposed to represent the hardness matching rate and as formulated:

$$R = \frac{H_{core}}{H_{outerlayer}} \tag{4}$$

where H_{core} and $H_{outer\ layer}$ denote the hardness of core and outer layer, respectively. While the calculated R for the as-fabricated composites and cryogenically treated composites are 0.73 and 0.47, respectively, it could be inferred that the incongruity of deformation exacerbates with decreasing hardness matching rate R. Since Fe–Ni–P outer layers become more rigid and hard to deform, the barreling effect of the core becomes more significant, which could have significant impact on the nominal stress and strain [24–26]. On the other hand, the failed cryogenically treated sample shows clear delamination around the outer ring of interface due to the intensive side folding effect, and early cracks are generated before complete destabilizing. Similar study conducted by using finite element method indicates that with the discrepancy of mechanical properties between components of a laminate increasing, stress and strain

concentrations become more significant [27]. Thus, it is necessary to take the matching of mechanical properties of components into account when designing composites.

4 Conclusion

In this study, Fe–Ni–P/porous-Fe/Fe–Ni–P composites were fabricated by the co-SPS process of Fe–N powder and Fe–Ni–P powder, and further strengthened by cryogenic treatment. Porous core forms as a result of the solid phase sintering and trapped gas, while the transient liquid phase sintering contributes to the densification of outer layers. During sintering, the liquid rearrangement promotes the atomic diffusion at interface, which is of significance to the complete combination. Low-temperature induced martensitic transformation from γ-Fe–Ni–P to α-Fe–Ni–P substantially improves the hardness of Fe–Ni–P layer (386.6 $HV_{0.1}$) and has no obvious impact on the porous-Fe core and the interface. However, the compressive strength dropped from 1708 to 1424 MPa after cryogenic treatment as a result of decreased hardness matching rate R. And with decreasing R, the incongruity of deformation exacerbates, which could cause the drop of compressive strength. The main contribution in the present work is to provide new guidance for the design of porous powder metallurgy products.

References

[1] L.P. Lefebvre, J. Banhart, D.C. Dunand, Adv. Eng. Mater. 10 (2008) 775–787.

[2] D.H. Yang, J.Q. Chen, W. Lei, J.H. Jiang, A.B. Ma, J. Iron Steel Res. Int. 25 (2018) 90–98.

[3] A.Y. Zaitsev, D.S. Wilkinson, G.C. Weatherly, T.F. Stephenson, J. Power Sources 123 (2003) 253–260.

[4] X.S. Wang, Z.L. Lu, L. Jia, J.X. Chen, J. Iron Steel Res. Int. 24 (2017) 97–102.

[5] G. Cui, X. Wei, E.A. Olevsky, R.M. German, J. Chen, Mater. Des. 90 (2016) 115–121.

[6] G. Cui, R. Jiang, A. Li, C. Zhang, J. Chen, Steel Res. Int. 89 (2018) 1700357.

[7] J. Banhart, H.W. Seeliger, Adv. Eng. Mater. 10 (2008) 793–802.

[8] P. Peng, K. Wang, W. Wang, L. Huang, K. Qiao, Q. Che, X. Xi, B. Zhang, J. Cai, Mater. Lett. 236 (2019) 295–298.

[9] C. Liu, Y. Liu, C.P. Liang, Y.Z. Ma, W.S. Liu, Y.L. Yang, Q.S. Cai, S.W. Tang, Mater. Sci. Technol. 35 (2019) 1583–1591.

[10] W. Chai, R.M. German, E.A. Olevsky, X. Wei, R. Jiang, G. Cui, Adv. Eng. Mater. 18 (2016) 1889–1896.

[11] R. Jiang, A. Li, G. Cui, C. Zhang, Metall. Mater. Trans. A 50 (2019) 2580–2584.

[12] G.D. Cui, R.J. Jiang, C.S. Zhang, Y.X. Liu, Metals 9 (2019) 785.

[13] A.D. Romig, J.I. Goldstein, Metall. Trans. A 11 (1980) 1151–1159.

[14] T.Y. Chan, S.T. Lin, J. Mater. Process. Technol. 89–90 (1999) 165–170.

[15] L. Kaufman, M. Cohen, JOM 8 (1956) 1393–1401.

[16] R.M. German, K.S. Churn, Metall. Trans. A 15 (1984) 747–754.

[17] K. Hayashi, T.W. Lim, Mater. Trans. JIM 32 (1991) 383–388.

[18] A.J. Markworth, Scripta Metall. 6 (1972) 957–960.

[19] R.M. German, P. Suri, S.J. Park, J. Mater. Sci. 44 (2009) 1–39.

[20] R.M. German, I. Smid, L.G. Campbell, J. Keane, R. Toth, Int. J. Refract. Met. Hard Mater. 23 (2005) 267–272.

[21] M.A. Dayananda, Y.H. Sohn, Metall. Mater. Trans. A 30 (1999) 535–543.

[22] S.K. Chaurasia, U. Prakash, V. Dabhade, Metall. Microstruct. Anal. 6 (2017) 561–568.

[23] K.D. Clarke, R.J. Comstock, M.C. Mataya, C.J. van Tyne, D.K. Matlock, Metall. Mater. Trans. A 39 (2008) 752–762.

[24] J.K. Banerjee, J. Eng. Mater. Technol. 107 (1985) 138–144.

[25] K.M. Kulkarni, S. Kalpakjian, J. Eng. Ind. 91 (1969) 743–754.

[26] R. Narayanasamy, R.S.N. Murthy, K. Viswanatham, G.R. Chary, J. Mech. Work. Technol. 16 (1988) 21–30.

[27] D.K. Kim, W. Woo, E.Y. Kim, S.H. Choi, J. Alloy. Compd. 774 (2019) 896–907.